Insights from a pseudospectral approach to the Elder problem

Maarten van Reeuwijk,[1] Simon A. Mathias,[1] Craig T. Simmons,[2] and James D. Ward[2]

Received 3 September 2008; revised 23 January 2009; accepted 9 February 2009; published 17 April 2009.

[1] The aim of this paper is to clarify and circumvent the issue of multiple steady state solutions in the Elder problem. A pseudospectral method is used to avoid numerical error associated with spatial discretization. The pseudospectral method is verified by comparison to an analytical solution at Rayleigh number, $Ra = 0$, and by reproducing the three stable steady state solutions that are known to exist at $Ra = 400$. A bifurcation diagram for $0 < Ra < 400$, which is free of discretization error, confirms that multiple steady states are indeed an intrinsic characteristic of the Elder problem. The existence of multiple steady states makes the $Ra = 400$ Elder problem less suitable for benchmarking numerical models. To avoid the multiple steady states, we propose a benchmark at $Ra = 60$. The results for this Low Rayleigh Number Elder Problem are presented and compared to simulations with the commercial groundwater modeling package FEFLOW. Correspondence between the pseudospectral model and FEFLOW is excellent.

Citation: van Reeuwijk, M., S. A. Mathias, C. T. Simmons, and J. D. Ward (2009), Insights from a pseudospectral approach to the Elder problem, *Water Resour. Res.*, *45*, W04416, doi:10.1029/2008WR007421.

1. Introduction

[2] The simulation of buoyancy driven flow (BDF) is frequently required in many areas of hydrology including saline contamination [*Zimmermann et al.*, 2006; *Bolster et al.*, 2007; *Narayan et al.*, 2007; *Lin et al.*, 2009] and more recently carbon sequestration [*Riaz et al.*, 2006; *Farajzadeh et al.*, 2007; *Hassanzadeh et al.*, 2007]. A major issue in BDF modeling is the problem of benchmarking [*Simpson and Clement*, 2003; *Simmons*, 2005; *Goswami and Clement*, 2007]. Typically, numerical models are verified by comparison with analytical solutions. Because of the nonlinear nature of BDF, analytical solutions often assume the existence of a sharp interface between heavy and light fluids [e.g., *Bear and Dagan*, 1964; *Huppert and Woods*, 1995; *Kacimov and Obnosov*, 2001] and are therefore unable to test a numerical model's ability to simulate buoyancy driven convective mixing. *Park* [1996] managed to relax this sharp interface assumption but at the expense of being restricted to one-dimensional flow only. More recently, *Dentz et al.* [2006] improved on this by deriving a perturbation-based analytical solution to the two-dimensional steady state problem of *Henry* [1964] [see also *Simpson and Clement*, 2004]. However, Henry's problem is also considered unsuitable in this context because the internal flow regime is driven by the hydraulic boundary conditions as opposed to buoyancy forces associated with variable density [*Simpson and Clement*, 2003]. Consequently, a popular method for benchmarking BDF models is to compare against published results from numerical solutions of the *Elder* [1967] problem [e.g., *Voss and Souza*, 1987; *Simpson and Clement*, 2003; *Soto Meca et al.*, 2007].

[3] The *Elder* [1967] problem originates from a heat convection experiment whereby a rectangular Hele-Shaw cell was heated over the central half of its base. A quarter of the way through the experiment, *Elder* [1967] observed six plumes, with four narrow plumes in the center and two larger plumes at the edges. As the experiment progressed, only four plumes remained. *Elder* [1967] also presented results from an equivalent but simplified numerical model. In contrast to the experiment, the model exhibited the development of a single plume only. These numerical results were subsequently reproduced by *Voss and Souza* [1987] using the USGS finite element code, SUTRA. The problem is that since then, there have been a significant number of published Elder problem simulations which dramatically vary in the way the plumes develop and the number of plumes that remain once the system has reached steady state [*Oldenburg and Pruess*, 1995; *Kolditz et al.*, 1997; *Ackerer et al.*, 1999; *Boufadel et al.*, 1999; *Oltean and Bues*, 2001; *Frolkovic and de Schepper*, 2000; *Diersch and Kolditz*, 2002]. These discrepancies have been attributed to various issues including mesh resolution, variation in numerical schemes and the use of different formulations for the governing equations [*Diersch and Kolditz*, 2002; *Woods et al.*, 2003; *Woods and Carey*, 2007; *Park and Aral*, 2007; *Al-Maktoumi et al.*, 2007]. More pertinently, using a bifurcation analysis based on a finite volume model, *Johannsen* [2003] demonstrated a consistent existence of three stable and a further eight unstable steady state solutions, significantly questioning the sensibility of using the Elder problem for benchmarking purposes.

[4] The aim of this paper is to provide a reproducible and accurate benchmark for the Elder problem, which does not suffer from the ambiguities mentioned above. To provide the most accurate numerical solution possible, we use a

[1]Department of Civil and Environmental Engineering, Imperial College London, London, UK.
[2]School of Chemistry, Physics and Earth Sciences, Flinders University, Adelaide, South Australia, Australia.

0043-1397/09/2008WR007421

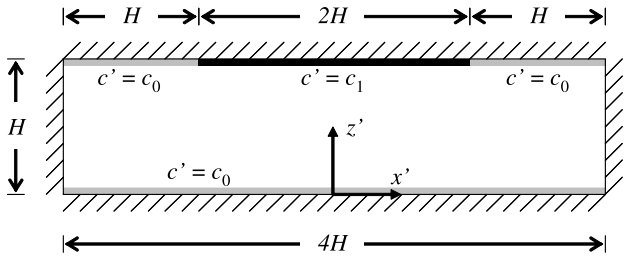

Figure 1. Schematic diagram of the problem geometry.

pseudospectral method based on sine and cosine series expansions in the horizontal direction and a Chebyshev expansion in the vertical. Pseudospectral methods are widely used in the study of transitional and turbulent flows [e.g., *Hussaini and Zang*, 1987], as they do not suffer from any numerical errors, except for the error associated with truncating the infinite series [*Boyd*, 2001; *Fornberg*, 1996]. *Wooding* [2007] provided a new analysis of the Salt Lake Problem [*Simmons et al.*, 1999; *Wooding et al.*, 1997] and suggested the future use of spectral methods in the solution of the transport equations used in simulating unstable variable density flows. The Salt Lake Problem is a test case which has been the subject of a very similar discussion to the Elder problem in terms of the current challenges faced by various numerical codes to accurately simulate BDF.

[5] The pseudospectral method is verified by comparing it to a new analytical solution of the purely diffusive Rayleigh Number $Ra = 0$ case, and by reproducing the three stable steady state solutions at $Ra = 400$. The resulting model is used to revisit the bifurcation analysis of *Johannsen* [2003] to gain insights into how the Elder problem can be improved as a benchmarking tool. The original Elder problem benchmark is at $Ra = 400$, which has multiple steady states. We propose a low Rayleigh number benchmark test case at a reduced $Ra = 60$ where only one steady state solution exists.

2. Governing Equations

[6] The governing equations, in dimensionless form, using the stream function formulation are (adapted from *Holzbecher* [1998] and *Al-Maktoumi et al.* [2007])

$$\frac{\partial c}{\partial t} + Ra\left(\frac{\partial \psi}{\partial z}\frac{\partial c}{\partial x} - \frac{\partial \psi}{\partial x}\frac{\partial c}{\partial z}\right) = \frac{\partial^2 c}{\partial x^2} + \frac{\partial^2 c}{\partial z^2} \tag{1}$$

$$\frac{\partial^2 \psi}{\partial x^2} + \frac{\partial^2 \psi}{\partial z^2} = \frac{\partial c}{\partial x} \tag{2}$$

Here, (1) is the prognostic equation for the concentration c [-], and (2) is the diagnostic equation governing the stream function ψ [-]. Furthermore,

$$x = \frac{x'}{H},\ z = \frac{z'}{H},\ t = \frac{D_E t'}{\phi H^2},\ c = \frac{c' - c_0}{c_1 - c_0} \tag{3}$$

and Ra [-] is the Rayleigh number found from

$$Ra = \frac{\alpha \rho_0 k g (c_1 - c_0) H}{\mu D_E}, \tag{4}$$

where x' [L] is horizontal distance, z' [L] is vertical distance, t' [T] is time, H [L] is the vertical extent of the system, ϕ [-] is porosity, D_E [L^2T^{-1}] is the effective diffusion coefficient, c' [ML^{-3}] is solute concentration, c_0 [ML^{-3}] is the freshwater solute concentration, c_1 [ML^{-3}] is the saltier water solute concentration, k [L^2] is permeability, g [LT^{-2}] is gravitational acceleration, μ [$ML^{-1}T^{-1}$] is dynamic viscosity and α [$M^{-1}L^3$] and ρ_0 [ML^{-3}] define the relationship between fluid density, ρ [ML^{-3}] and solute concentration c', given by

$$\rho = \rho_0(1 + \alpha(c' - c_0)) \tag{5}$$

[7] The domain and boundary conditions for the Elder problem are illustrated in Figure 1. As the governing equations and boundary conditions are symmetric, it suffices to consider the right-half plane $[0, 2] \times [0, 1]$, for which the boundary conditions are

$$\begin{aligned}
&\psi = 0, \quad 0 \le x \le 2, \quad 0 \le z \le 1, \quad t = 0\\
&\psi = 0, \quad 0 \le x \le 2, \quad z = 0, \quad t > 0\\
&\psi = 0, \quad 0 \le x \le 2, \quad z = 1, \quad t > 0\\
&\psi = 0, \quad x = 0, \quad 0 \le z \le 1, \quad t > 0\\
&\psi = 0, \quad x = 2, \quad 0 \le z \le 1, \quad t > 0
\end{aligned} \tag{6}$$

$$\begin{aligned}
&c = 0, \quad 0 \le x \le 2, \quad 0 \le z \le 1, \quad t = 0\\
&c = 0, \quad 0 \le x \le 2, \quad z = 0, \quad t > 0\\
&c = f(x), \quad 0 \le x \le 2, \quad z = 1, \quad t > 0\\
&\frac{\partial c}{\partial x} = 0, \quad x = 0, \quad 0 \le z \le 1, \quad t > 0\\
&\frac{\partial c}{\partial x} = 0, \quad x = 2, \quad 0 \le z \le 1, \quad t > 0
\end{aligned} \tag{7}$$

$$f(x) = \begin{cases} 1, & 0 \le x \le 1 \\ 0, & 1 < x \le 2 \end{cases} \tag{8}$$

3. Numerical Procedure

[8] The first step is to expand ψ and c in the horizontal direction such that

$$\psi(x, z, t) = \sum_{m=1}^{M} \hat{\psi}_m(z, t) \sin(k_m x) \tag{9}$$

$$c(x, z, t) = \sum_{m=0}^{M} \hat{c}_m(z, t) \cos(k_m x) \tag{10}$$

where $k_m = m\pi/2$. The choice of sin and cos for ψ and c relates to their horizontal boundary conditions (recall Dirichlet and Neumann respectively).

[9] We now invoke the horizontal and vertical dimensionless Darcy fluxes

$$q_x = \frac{\partial \psi}{\partial z},\ q_z = -\frac{\partial \psi}{\partial x} \tag{11}$$

such that equation (1) can be rewritten as

$$\frac{\partial c}{\partial t} + Ra\left(\frac{\partial}{\partial x}(q_x c) + \frac{\partial}{\partial z}(q_z c)\right) = \frac{\partial^2 c}{\partial x^2} + \frac{\partial^2 c}{\partial z^2} \tag{12}$$

[10] From equations (9) and (11) it can be seen that q_x will be odd in x whereas q_z will be even. Therefore, corresponding expansions for the products $q_x c$ and $q_z c$ should be written as

$$q_x c(x,z,t) = \sum_{m=1}^{M} \widehat{q_x c}_m(z,t)\sin(k_m x) \tag{13}$$

$$q_z c(x,z,t) = \sum_{m=0}^{M} \widehat{q_z c}_m(z,t)\cos(k_m x) \tag{14}$$

[11] Substituting equations (9), (10), (13) and (14) into equations (2) and (12) and using orthogonality of basis functions then leads to

$$\frac{\partial \hat{c}_m}{\partial t} + Ra\left(k_m \widehat{q_x c} + \frac{\partial \widehat{q_z c}_m}{\partial z}\right) = -k_m^2 \hat{c}_m + \frac{\partial^2 \hat{c}_m}{\partial z^2} \tag{15}$$

and

$$-k_m^2 \hat{\psi}_m + \frac{d^2 \hat{\psi}_m}{dz^2} = -k_m \hat{c}_m \tag{16}$$

Note that this transformation, once $\widehat{q_x c}_m$ and $\widehat{q_z c}_m$ have been determined, has decoupled equations (1) and (2) in the x direction, so that each mode m can be solved independently of the other modes.

[12] To numerically evaluate the above problem the first step is to approximate the cosine and sine transforms and corresponding inverses with their discrete counterparts. We choose to use DCT-I and DST-I, and their corresponding inverses, IDCT-I and IDST-I, which can be efficiently implemented using Fast Fourier transforms (FFT) [see *Martucci*, 1994]. In this way it can be said that

$$\hat{\psi}_m(z,t) = \text{DST-I}[\psi(x_m,z,t)],$$

$$c_m(z,t) = \text{DCT-I}[c(x_m,z,t)],$$

$$\widehat{q_x c}_m(z,t) = \text{DST-I}[q_x c(x_m,z,t)],$$

$$\widehat{q_z c}_m(z,t) = \text{DCT-I}[q_z c(x_m,z,t)],$$

$$q_z(x_m,z,t) = \text{IDCT-I}\left[-k_m \hat{\psi}_m(z,t)\right],$$

where

$$x_m = \frac{2m}{M},\ m = 0,1\ldots M \tag{17}$$

It should be noted that the DCT-I and DST-I methods correspond to cosine and sine transforms up to a prefactor [*Martucci*, 1994]. These prefactors should be applied before there is full correspondence.

[13] In the z direction, the nonperiodicity of the boundary conditions suggests the use of an expansion in Chebyshev polynomials, T_k [*Boyd*, 2001, p. 10]:

$$p(\xi) = \sum_{k=0}^{N} \tilde{p}_k T_k(\xi) \tag{18}$$

where [*Boyd*, 2001, p. 497]

$$T_0(\xi) = 1, T_1(\xi) = \xi, T_{k+1}(\xi) = 2\xi T_k(\xi) - T_{k-1}(\xi) \tag{19}$$

The Chebyshev polynomials form a basis on the interval $-1 \le \xi \le 1$ which can be mapped to z using the transformation $\xi = 2z - 1$. In physical space, the variables are defined at the points

$$z_n = \frac{\xi_n + 1}{2},\ \xi_n = \cos\left(\frac{n\pi}{N}\right),\ n = 0,1\ldots N \tag{20}$$

where ξ_n are known as the Chebyshev-Gauss-Lobatto points. With this choice of collocation points, the nodal values of $p(\xi_n)$ and the Chebyshev coefficients $\tilde{p}_k$ are related by a discrete cosine transform (See Appendix A). The strong clustering of points near the top and bottom wall is advantageous because of the large near-wall gradients in the Elder problem.

[14] The relationship of the Chebyshev coefficients of p in (18) and its first derivative

$$\frac{dp}{d\xi} = \sum_{k=0}^{N} \tilde{p}_k^{(1)} T_k(\xi). \tag{21}$$

is given by

$$\begin{bmatrix} \tilde{p}_0^{(1)} \\ \tilde{p}_1^{(1)} \\ \vdots \\ \tilde{p}_{N-1}^{(1)} \\ \tilde{p}_N^{(1)} \end{bmatrix} = \mathbf{D}_\xi \begin{bmatrix} \tilde{p}_0 \\ \tilde{p}_1 \\ \vdots \\ \tilde{p}_{N-1} \\ \tilde{p}_N \end{bmatrix} \tag{22}$$

where $\mathbf{D}_\xi$ is a $N+1 \times N+1$ sparse upper diagonal differentiation matrix given by (see Appendix A)

$$\mathbf{D}_\xi = \begin{bmatrix} 0 & 1 & 0 & 3 & 0 & 5 & \ldots & N \\ 0 & 0 & 4 & 0 & 8 & 0 & \ldots & 0 \\ \vdots & & \ddots & 6 & 0 & 10 & \ldots & 2N \\ \vdots & & & \ddots & \ddots & \ddots & \ddots & \\ \vdots & & & & \ddots & \ddots & \ddots & 2N \\ \vdots & & & & & \ddots & \ddots & 0 \\ \vdots & & & & & & \ddots & 2N \\ 0 & & \ldots & \ldots & \ldots & \ldots & & 0 \end{bmatrix} \tag{23}$$

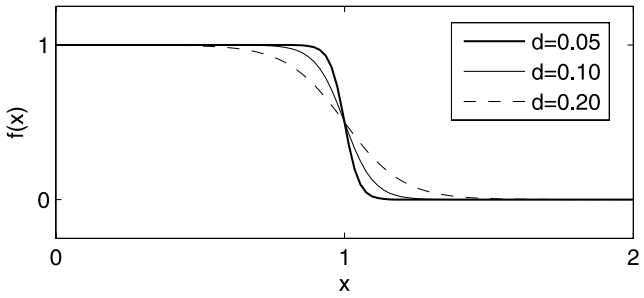

Figure 2. Smoothed boundary condition at $z = 1$.

Note that the last row of $\mathbf{D}_\xi$ contains zeros only. This is significant for enforcing the boundary conditions for ODEs with the so-called tau method.

[15] The coefficients for the fully expanded (in both x and z) functions of c, ψ, $q_x c$ and $q_z c$ are denoted by $\tilde{c}_{m,n}$, $\tilde{\psi}_{m,n}$, $\tilde{a}_{x;m,n}$ and $\tilde{a}_{z;m,n}$, respectively. With a point distribution according to equation (20), these coefficients can be obtained using the discrete cosine transform DCT-I (see Appendix A)

$$\tilde{\psi}_{m,n}(t) = \text{DCT-I}\left[\hat{\psi}_m(z_n,t)\right]$$

$$\tilde{c}_{m,n}(t) = \text{DCT-I}[\hat{c}_m(z_n,t)]$$

$$\tilde{a}_{x;m,n}(t) = \text{DCT-I}[\widehat{q_x c}_m(z_n,t)]$$

$$\tilde{a}_{z;m,n}(t) = \text{DCT-I}[\widehat{q_z c}_m(z_n,t)]$$

In the expressions above, the prefactors have been omitted [see *Martucci*, 1994].

[16] As discussed before, each mode m can be solved independently of the other modes. Therefore, when these coefficients are grouped per mode m in the vectors $\tilde{\mathbf{c}}_m = [\tilde{c}_{m,0}\ldots\tilde{c}_{m,N}]^T$, $\tilde{\boldsymbol{\psi}}_m = [\tilde{\psi}_{m,0}\ldots\tilde{\psi}_{m,N}]^T$, $\tilde{\mathbf{a}}_{x;m} = [\tilde{a}_{x;m,0}\ldots\tilde{a}_{x;m,N}]^T$ and $\tilde{\mathbf{a}}_{z;m} = [\tilde{a}_{z;m,0}\ldots\tilde{a}_{z;m,N}]^T$, the resulting system of equations can be compactly written as

$$\frac{d\tilde{\mathbf{c}}_m}{dt} = -Ra\left(k_m\tilde{\mathbf{a}}_{x;m} + \mathbf{D_z}\tilde{\mathbf{a}}_{z;m}\right) + \left(\mathbf{D_{zz}} - k_m^2\mathbf{I}\right)\tilde{\mathbf{c}}_m, \qquad (24)$$

and

$$\left(\mathbf{D_{zz}} - k_m^2\mathbf{I}\right)\tilde{\boldsymbol{\psi}}_m = -k_m\tilde{\mathbf{c}}_m \qquad (25)$$

where $\mathbf{I}$ is the identity matrix, and $\mathbf{D_z}$ and $\mathbf{D_{zz}}$ are the first- and second-order differentiation matrices with respect to z, respectively. These matrices are connected to $\mathbf{D}_\xi$ in (23) by a simple coordinate transform: $\mathbf{D_z} = \mathbf{D}_\xi d\xi/dz$ and $\mathbf{D_{zz}} = \mathbf{D}_\xi^2(d\xi/dz)^2$ (see Appendix A). In our case, $d\xi/dz = 2$.

[17] The model solves for $\tilde{c}_{m,n}$ by time integrating (24). Using equation (25), the coefficients $\tilde{\psi}_{m,n}$ can immediately be expressed in terms of $\tilde{c}_{m,n}$ through the inverse of the discrete differential operator. At each time step, the coefficients of the nonlinear terms $\tilde{a}_{x;m,n}$ and $\tilde{a}_{z;m,n}$ need to be recomputed. This is done by mapping $\tilde{\psi}_{m,n}$ and $\tilde{c}_{m,n}$ to physical space, calculating the products $q_x c$ and $q_z c$, and converting back to the functional space. As discussed, the mapping between the physical and functional space is achieved using discrete sine and cosine transforms. The boundary conditions are enforced via the tau method, and are discussed in more detail in Appendix A.

[18] For transient simulations, time integration can be accurately achieved using the stiff integrator ODE15S available in any standard version of MATLAB [*Shampine and Reichelt*, 1997; *Shampine et al.*, 1999]. Although ODE15S is used for the smaller simulations, the method becomes prohibitively expensive when M and N become large. This is caused in particular by the strong clustering toward the walls in the z direction, which makes the eigenvalues of the discrete diffusion operator very large; consequently, extremely small time steps will be required. Therefore, a more efficient approach is to use an implicit-explicit procedure to obtain the highly resolved steady state solutions of sections 4 and 5, where diffusion is discretized by an Euler backward scheme, and advection by an Euler forward scheme. This standard operator-splitting procedure is unconditionally stable for the diffusion, so that physically more relevant time steps can be used. Note that the first-order accuracy of the Euler scheme is no concession to the spectral accuracy of the method, when this scheme is used to find steady state solutions.

[19] Spectral methods can produce accurate solutions with relatively few modes, because of an exponential convergence to the exact solution. However, the solution has to be sufficiently smooth; when the solution is not smooth, convergence can be much weaker, as Gibbs phenomena may prevent pointwise convergence near discontinuities [*Trefethen*, 2000, p. 15]. In the Elder problem, there is a discontinuity in the boundary condition at the top wall, as given in (8). To have control over the sharpness of the transition (and hence the local convergence), (8) is replaced by

$$f(x) = \frac{1}{2}\left[1 - \tanh\left(\frac{x-1}{d}\right)\right] \qquad (26)$$

Here, d represents a transition length: the larger d, the smoother the transition. Clearly, as $d \to 0$, the original boundary condition (8) is recovered (see also Figure 2). The influence of d on the solutions of the Elder problem is discussed in Appendix B. A useful byproduct of replacing equation (8) by (26) is that grid-independent solutions exist: sufficiently close to a discontinuity at the top wall, a numerical solution will never converge because the local gradients become steeper each time the grid is refined. One might even question the physical relevance of equation (8) in itself, as the discontinuity locally induces infinite fluxes, which cannot exist in reality.

4. Verification

[20] The pseudospectral code is verified in two ways: by a comparison to an analytical solution at $Ra = 0$ and to the three stable steady state solutions at $Ra = 400$, as identified by *Johannsen* [2003]. The analytical solution to equations (1)–(7) at $Ra = 0$ is derived in Appendix C using a cosine transform in the x direction and a Laplace transform for t. The solution is given by

$$\bar{c}(x,z,s) = \frac{\sinh\left(s^{1/2}z\right)}{2s\sinh\left(s^{1/2}\right)} + \sum_{m=1}^{\infty}\frac{\sin(g_m)\sinh(\lambda_m z)\cos(g_m x)}{sg_m\sinh(\lambda_m)}. \qquad (27)$$

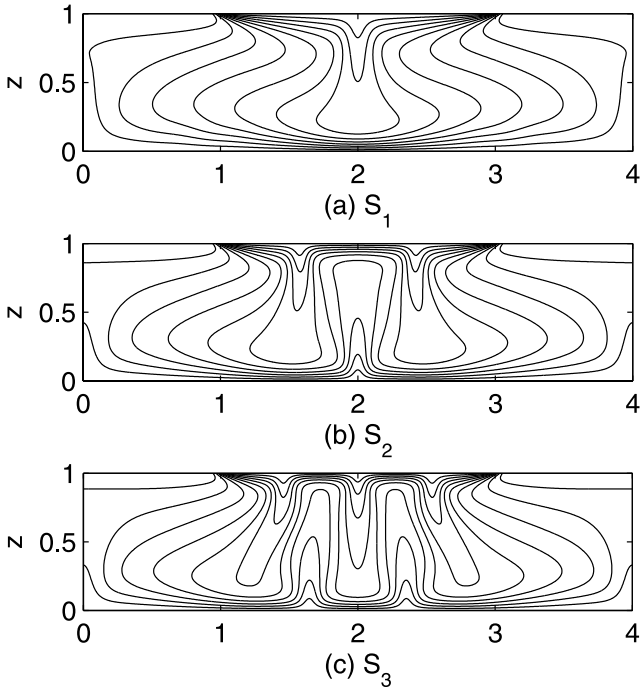

Figure 3. The three steady state solutions at $Ra = 400$, obtained by using different initial conditions.

Here, s is the Laplace variable such that $\bar{c}(s) = \int_0^\infty c(t)e^{-st}dt$. Equation (27) can be inverted numerically using the *Stehfest* [1970] algorithm [see also *Valko and Abate*, 2004].

[21] The analytical solution at $Ra = 0$ at $t = 0.03$, 0.1, 0.3 and 1.0 is shown in Figures 7a–7d, respectively. Plotted in Figures 7a–7d are the solutions from the pseudospectral method for 97 × 33 modes. The value for d has been set to $d = 0.005$, which is too small a value for pointwise convergence very close to $x = \pm 1$. However, at this resolution, the solution is globally converged, even at $Ra = 400$, as will be demonstrated in the convergence study below. The overall accuracy is evident from the excellent agreement with the analytical solution in Figures 7a–7d.

[22] Next, the three stable steady state simulations at $Ra = 400$ (the original benchmark value for Ra), identified by *Johannsen* [2003], will be reproduced with the pseudospectral method. For this simulation, d is set to 0.05, for which pointwise convergence is achieved at 513 × 129 modes. This value of d is sufficiently small to capture the important characteristics of the original Elder problem, as shown below and in Appendix B.

[23] The three stable steady state solutions at $Ra = 400$ found with the pseudospectral method are shown in Figure 3. The steady state solutions are denoted by S_1, S_2 and S_3, where the subscript represents the number of downward plumes in the solution. Figure 3 shows the isolines of concentration with $\Delta c = 0.1$. The transient behavior leading to the steady state are very similar to those reported by *Park and Aral* [2007] and *Woods and Carey* [2007] and will not be shown here. For these simulations, a steady state was reached at $t = 0.5$ (which corresponds to 200 convective time units when $Ra = 400$).

[24] Steady state solutions S_1 and S_2 were found quite easily, by using initial conditions of the form $c(x, z, 0) = C\,(1 - (-1)^m \cos(\pi m x))/2$ for $0 < x < 1$, where m is an integer. For $x > 1$, $c(x, z, 0) = 0$. By varying m and C, the simulation usually ends up either in S_1 or S_2. However, S_3 cannot be found this way. In fact, we were unable to independently obtain S_3, despite trying a large set of initial conditions (varying m, C, d, trying different z dependencies for $c(x, z, 0)$, adding white noise). In the end, we digitized the concentration isolines of the S_3 solution by *Johannsen* [2003]. The two-dimensional field for c was then reconstructed by solving the system $\nabla^2 c = 0$ with Gauss-Seidel iterations (a Laplace equation is a good interpolator), subject to the boundary conditions and the internal constraints imposed by the isolines. This resulted in an approximation of the S_3 solution, which was then used as an initial condition for the pseudospectral method. With this initial condition, the end result was indeed S_3, as presented in Figure 3c. Apparently, the basin of attraction of S_3 is small; only a small subset of initial conditions leads to S_3.

[25] A particularly good indicator for the system, as well as the pointwise convergence of the solution, is the vertical solute flux at the top wall. The vertical solute flux at $z = 1$ will be referred to as the local Sherwood number Sh_x, given by

$$Sh_x(x) = \left.\frac{dc}{dz}\right|_{z=1}. \tag{28}$$

Furthermore, the average Sherwood number Sh is defined as

$$Sh = \frac{1}{2}\int_0^2 Sh_x dx. \tag{29}$$

[26] In Figure 4, Sh_x is shown for the three stable steady state solutions. All solutions have a sharp peak in Sh_x at $x = \pm 1$, which is caused by the sharp transition of c in the boundary condition. The smaller d is, the sharper this peak will be. The reason for the peak is that the sharp transition drives a strong flow past the walls toward the center of the domain, as may be inferred from the presence of $\partial c/\partial x$ in equation (2). This flow transports fluid with a low concentration past the plate. As a result, Sh_x near $x = \pm 1$ becomes very large.

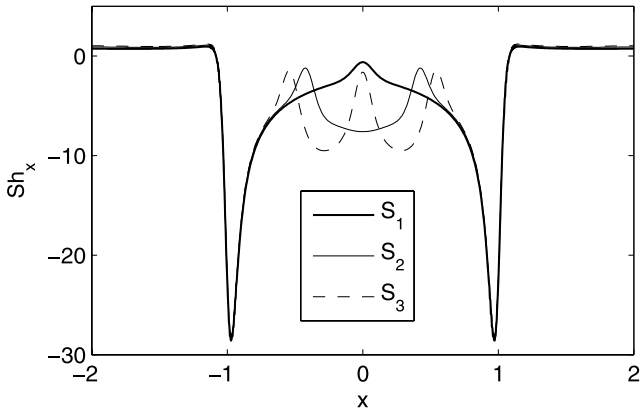

Figure 4. The vertical solute flux Sh_x for the three steady states.

Table 1. Resolutions Used for the Convergence Study of the Pseudospectral Method

Simulation	N_x	N_z
1	25	13
2	29	15
3	33	17
4	65	25
5	97	33
6	129	41
7	193	49
8	257	65
9	385	97
10	513	129

[27] At the location of a downward plume, Sh_x is reduced, while an upward plume causes an increase in Sh_x. As S_1, S_2 and S_3 differ in the number of the downward and upward plumes, their Sh_x profile will differ in the number of maxima and minima. Consequently, Sh differs as well. Indeed, at $Ra = 400$, Sh is 3.5, 4.0 and 4.2 for solution S_1, S_2 and S_3, respectively. This distinguishing property will be used for the bifurcation diagram in section 5.

[28] While pointwise convergence is reached at 513 × 129 modes for $d = 0.05$, global convergence, i.e., convergence in a norm, is achieved much faster. Table 1 lists the resolutions of ten simulations that have been used for a convergence study. The high-resolution solution S_1 (Figure 3a) has been used as the initial condition for all simulations, and equations (24) and (25) were integrated with the Euler implicit-explicit scheme until a steady state was reached. Simulation 1 was the coarsest simulation that converged. The obtained steady state solutions of the concentration field $c^{(n)}$ are compared to the concentration field $c^{(\mathrm{ref})}$ at the highest resolution (513 × 129), and the error $\epsilon^{(n)}$ is calculated according to

$$\epsilon^{(n)} = \frac{\int |c^{(n)} - c^{(\mathrm{ref})}| dA}{\int dA} \tag{30}$$

[29] The fast convergence of the pseudospectral method is evident in Figure 5. The error falls approximately with an exponent −6 up to a resolution of 97 × 33, where the error is $O(10^{-5})$. At higher resolutions, the convergence becomes nonuniform, which is caused by the nonequidistant mapping in the z direction. When no interpolation is needed to compare with the reference simulation (i.e., when N_z is 17, 33, 65), the error relative to the fully resolved simulation is lower.

5. Bifurcation Behavior

[30] Traditionally, the Elder problem has primarily been used for benchmarking purposes. As a result, most studies considered $Ra = 400$ only, and remarkably little was known of the behavior of the solutions at lower Ra. Only recently, *Johannsen* [2003] used a finite volume code combined with a pseudo-arclength continuation method to construct a bifurcation diagram of the Elder problem for $0 < Ra < 400$. The study identified three stable solutions and an additional eight unstable solutions, and showed that S_2 and S_3 (and their unstable counterparts) come into existence via a saddle node (fold) bifurcation. In constructing a bifurcation diagram, one has to characterize an entire solution by a single number. *Johannsen* [2003] used a projection of the solution which maximized the difference between the different solution branches. In this study, the average Sherwood number Sh is used; as discussed in section 4, Sh is a good indicator to distinguish between S_1, S_2 and S_3.

[31] The bifurcation diagram (Figure 6) was obtained by using each of the three steady state solutions S_1, S_2 and S_3 at $Ra = 400$ as initial conditions for a simulation at $Ra = 390$. This simulation was then run for 100 convective time units (which corresponds to $t = 100/Ra$ diffusive time units) until steady state was reached. Sh was calculated, and the new steady state solution was used as the initial condition $Ra = 380$ and so on. Near the bifurcation points the Ra intervals were reduced to 1 to capture the bifurcation properly. When S_2 and S_3 cease to exist at their respective bifurcation points, the flow solution converges to S_1. The bifurcation points are denoted by circles in Figure 6.

[32] Figure 6 shows the bifurcation diagram for the Elder problem for $0 < Ra < 400$. The only solution which exists for the entire range of Ra is S_1. From $Ra = 76$ onwards, S_2 comes into existence via a fold bifurcation. Similarly, S_3 comes into existence at $Ra = 172$. An interesting detail is that near the bifurcation points, Sh for S_2 and S_3 is lower than for S_1. Sufficiently far away from the bifurcation points, solutions with more plumes have a higher Sh. The

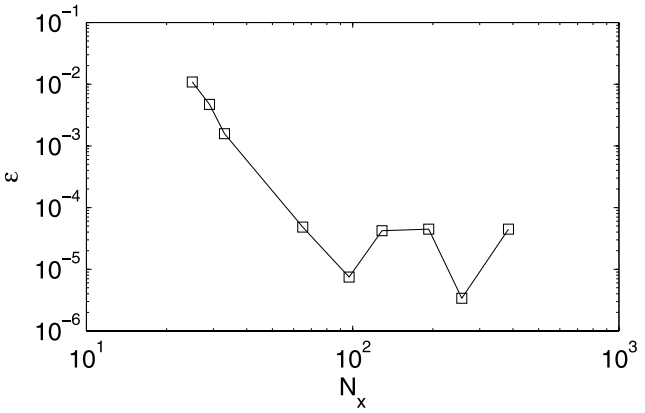

Figure 5. Convergence behavior of the pseudospectral method.

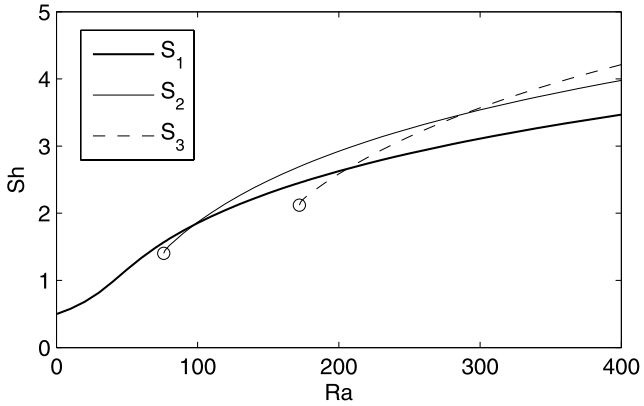

Figure 6. Bifurcation diagram of the Elder problem for $0 < Ra < 400$.

bifurcation points are comparable with *Johannsen* [2003], who reports that S_2 and S_3 come into existence at $Ra = 67$ and $Ra = 151$, respectively. The slight differences are most likely caused by the different numerical methods.

[33] It should be noted that there may be more than three stable steady state solutions at $Ra = 400$. Indeed, the pseudo-arclength continuation method used by *Johannsen* [2003] provides a systematic way to follow the solutions as Ra changes, but does not guarantee that all solutions are found. Hence, it is imaginable that more than three stable steady solutions exist. If they exist, these steady states will have tiny basins of attraction, as they have not been stumbled upon before.

[34] For the Elder problem, the onset of convection as characterized by the critical Rayleigh number Ra_c, is at $Ra_c = 0$. This is clear from Figure 6, as Sh steadily increases from $Sh = 1/2$ (the diffusive state) for $Ra > 0$. This behavior is different from the classical value of $Ra_c = 4\pi^2$ for an infinitely extending strip with constant boundary conditions [*Horton and Rogers*, 1945]. The difference in Ra_c originates from the difference in boundary conditions. For the Elder problem, the finite length of the $c = 1$ boundary condition generates a concentration gradient $\partial c/\partial x$ near $x = \pm 1$. The existence of a concentration gradient will drive a flow, as is evident in equation (2). As this gradient cannot be undone by diffusive transport as is the case for the infinite strip, convection will occur for every $Ra > 0$.

[35] Figure 6 clearly elicits the reason for the ambiguities in using the Elder problem as a benchmark: at $Ra = 400$, three stable steady state solutions coexist. As a result, some regions of the space of initial conditions will converge to S_1, other regions to S_2 and yet others to S_3. These regions may be intertwined and even have fractal boundaries. Moreover, the governing equations, the numerics and the grid resolution will affect the shape and extent of these regions. Hence, the ambiguities with the Elder problem are physical rather than numerical.

[36] However, a pragmatic solution to the coexistence of stable steady state solutions is also evident in Figure 6; simply lower Ra. Indeed, for $Ra < 76$, the Elder problem has a single steady state solution. Hence, all initial conditions should converge to S_1 for $Ra < 76$, so that the details of the governing equations, numerics and grid resolution become much less crucial.

6. Low Rayleigh Number Elder Problem

[37] The original Elder problem is formulated for a Rayleigh number of $Ra = 400$. We have seen that three steady state solutions exist for the Elder problem: S_1, S_2 and S_3. It has also been demonstrated that the Elder problem has only one steady state solution for $Ra < 76$. It is therefore useful to develop a test case version of the Elder problem at reduced Rayleigh number in the regime where only one steady state solution exists. As we would like to be sufficiently far from the bifurcation point, we choose $Ra = 60$ as a new test case. We coin this new test case the Low Rayleigh Number Elder Problem. At this Ra, all flow solutions should converge to S_1. Although the buoyancy force at $Ra = 60$ is far less than at $Ra = 400$, transport by convection remains significant. The $Ra = 60$ benchmark is therefore suitable for verification purposes. In addition, it can be used to study the accuracy of the diffusive and convective discretizations, as well as the time integration scheme.

[38] We compare results at $Ra = 60$ of the new pseudospectral method with results from a standard variable density groundwater flow and solute transport model. For this purpose, FEFLOW version 5.3 [*Diersch*, 2005] was used. *Diersch* [2005] provides exhaustive information relating to the FEFLOW variable density groundwater flow model. FEFLOW employs the fundamental physical principles of fluid mass conservation, solute mass conservation and momentum conservation. It has been successfully tested on numerous benchmarks, including those reported for variable density flow, the details of which are given by *Diersch and Kolditz* [2002] and *Diersch* [2005].

[39] The standard Elder problem (high Rayleigh number case of $Ra = 400$) was initially reproduced with FEFLOW. The details of this problem are reported in a vast body of literature and are not reproduced here. See *Diersch and Kolditz* [2002, Table 1] for a complete listing of parameters used in the benchmark Elder problem case for $Ra = 400$ and a complete discussion on the results of the standard test case. We modified this base case problem by adjusting the left hand and right hand portions of the top boundary adjacent to the solute source in order to be completely consistent with the boundary conditions used in the pseudospectral method (Figure 1). This involved changing the top boundary condition to include a constant concentration boundary of value $c' = c_0$ along the top boundary either side of the solute source ($c' = c_1$) present in the center of the top boundary. Hence, the FEFLOW simulations uses the original boundary condition (26), so that the transition length d is set implicitly by the horizontal mesh spacing at $x = \pm 1$. Note here that in the FEFLOW simulation we simulate the full plane solution (total horizontal dimension = 600 m) in order to ensure that the half plane solution used elsewhere throughout this study is justifiable. There are well known examples in turbulence problems where governing equations and boundary conditions feature symmetries but their solutions do not. A simple example where the symmetry breaks down is the problem of flow past a circular cylinder [*Frisch*, 1995]. Our results confirm that the half plane solution and the full plane solution are entirely consistent. To lower the Rayleigh number of the system to $Ra = 60$, the density contrast between the solute source and the ambient initial fluid was reduced. This was achieved by reducing the concentration value of the upper solute source boundary (originally $c' = c_1 = 1$) to a new reduced value of $c' = c_1 = 60/400$. Two grid discretizations are presented here: coarse utilizing 4,539 nodes (horizontal nodes = 89; vertical nodes = 51) and fine utilizing 17,877 nodes (horizontal nodes = 177; vertical nodes = 101). A sensitivity analysis to spatial discretization utilizing both coarser and finer grids ensured that the model results presented here were grid-independent and confirmed that the above spatial discretization was satisfactory. Time stepping in FEFLOW is regulated through the use of an automatic time step increment. The choice of time step size is regulated by error checking (based on a Euclidean L2 integral (RMS) error norm of 10^{-3}) and the use of Courant type stability criteria. Simulations were run in transient mode for 200 years simulated real time to reach a steady

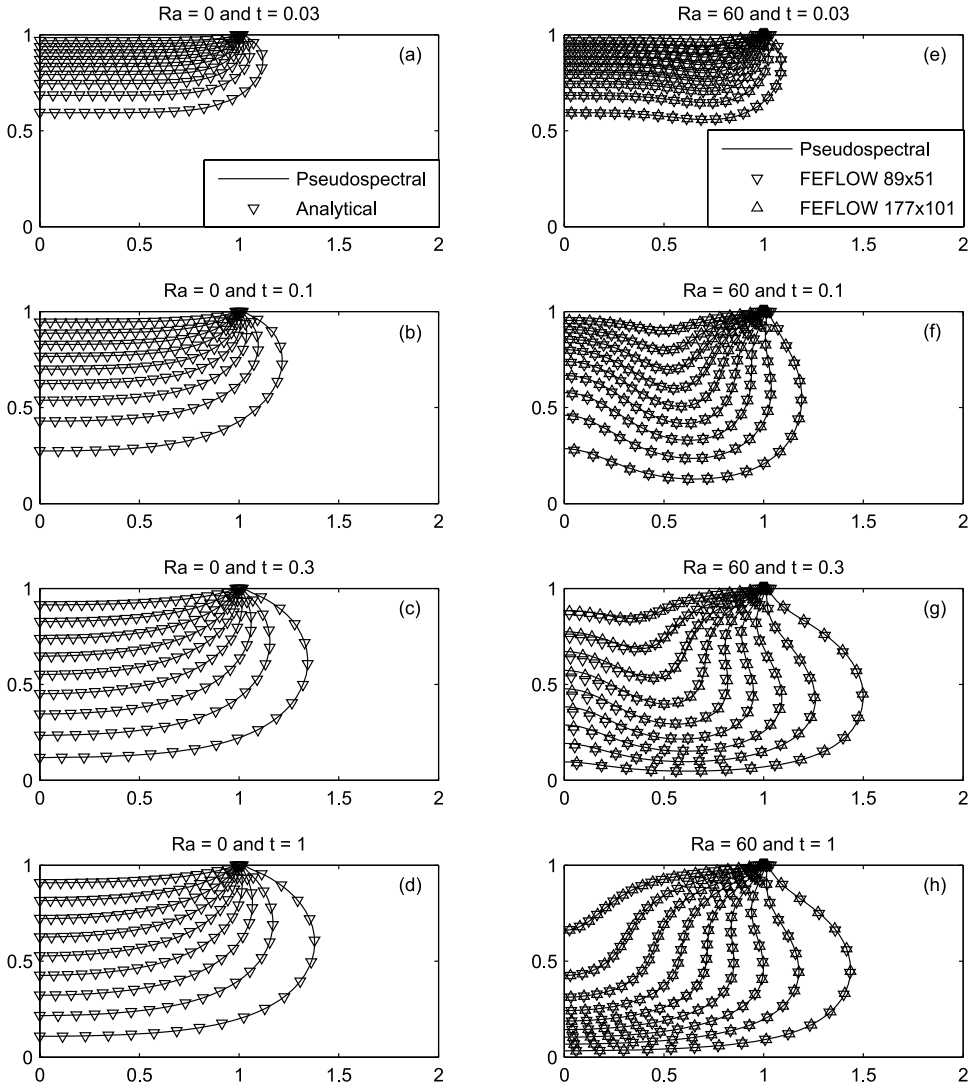

Figure 7 Isolines of the concentration field for $t = 0.03$, $t = 0.1$, $t = 0.3$ and $t = 1.0$ at $Ra = 0$ and $Ra = 60$. (a)–(d) Comparison of the pseudospectral method (solid line) to the new analytical solution at $Ra = 0$ (downward triangles). (e)–(h) Comparison of FEFLOW simulations with 89×51 (downward triangles) and 177×101 nodes (upward triangles) to the pseudospectral method (solid line).

state solution. The original Elder problem $Ra = 400$ solutions are usually reported for timescales that are much shorter, typically on the order of 20 years.

[40] For the pseudospectral method, 97×33 modes were employed, and the upper boundary condition (26) used a value of $d = 0.005$. As for the $Ra = 0$ solution, this value of d is too low to achieve pointwise convergence very near the boundaries at $x = \pm 1$. However, as shown in the convergence study, the solution has fully converged globally. Results comparing the pseudospectral method and the FEFLOW simulations are shown in Figures 7e–7h for dimensionless time $t = 0.03$, 0.1, 0.3, and 1. These correspond to real time values of 6, 20, 60 and 200 years, respectively, on the basis of scaling relations provided in equation (3). Results show excellent agreement between the pseudospectral method and the FEFLOW simulations with both the fine and coarse grid resolutions. The coarse grid simulation is slightly off in Figure 7g, but the fine grid simulation has converged to the prediction of the pseudospectral method.

7. Concluding Remarks

[41] There has been much discussion in recent literature about the Elder Problem and the discrepancy between various numerical simulations in terms of the number of convection cells and the development of unstable plumes. A number of factors have been highlighted which appear to explain, at least in part, the various discrepancies. These include different mesh resolutions, different formulations of the governing flow and transport equations, and different numerical solution schemes.

[42] However, the underlying cause of these discrepancies is not numerical but physical; at $Ra = 400$, there are at least three stable steady state solutions, S_1, S_2, and S_3, as was shown in the bifurcation analysis of *Johannsen* [2003]. This point has been largely ignored in the plethora of Elder

problem benchmark studies. Because of the existence of multiple steady state solutions, the phase space will be partitioned: some initial conditions will generate trajectories which lead to S_1, while others lead to S_2 and yet others to S_3. There may even be more than three stable solutions, although these have not yet been found. The basins of attraction of S_1, S_2 and S_3 are intertwined and may have fractal boundaries, so that slight variation of the initial conditions may lead to different steady states. It would be useful for the Elder experiments to be repeated to check whether these different steady states can be reproduced in the laboratory.

[43] Differences in the governing equations, grid resolution and the employed discretization techniques will affect the size and shape of the basins of attraction for the stable solutions. Hence, even when using the same initial conditions, different codes may yield different steady states. In this study, we aimed to eliminate all sources of numerical discrepancy, in order to get uncontaminated insight into the ambiguities associated with the Elder problem benchmark. For this reason, a pseudospectral method was employed with sine and cosine series expansions in the horizontal, and Chebyshev series expansions in the vertical. The key results of this study are as follows.

[44] 1. The pseudospectral method has been successfully used to simulate the Elder problem for a range of Rayleigh numbers including the original base test case at $Ra = 400$.

[45] 2. Using the pseudospectral method, we find excellent agreement with a new analytical solution for the purely diffusive case at $Ra = 0$. We note that the critical Rayleigh number for the Elder problem is $Ra = 0$, above which fluid motion due to convection begins for any nonzero value of the unstable concentration difference.

[46] 3. We have successfully used the pseudospectral method to reproduce the three stable steady state solutions at $Ra = 400$ reported previously by *Johannsen* [2003] in his bifurcation analysis. Depending on the initial conditions, grid resolution, governing equations and discretization, the final solution to the Elder problem is seen to converge to one of three possible steady solutions S_1, S_2 and S_3. Since multiple steady solutions exist to the Elder problem, this calls into question the usefulness of the $Ra = 400$ version of the Elder problem as a model benchmark. Multiple solutions make intercode comparisons cumbersome. Because of sensitive dependence of the flow evolution upon initial conditions, grid resolution, governing equations and discretization, the flow solution may either be S_1, S_2 or S_3. At the very least, it suggests that the original $Ra = 400$ Elder problem benchmark should be used with caution and careful interpretation.

[47] 4. Our bifurcation analysis shows that S_1 exists for $0 < Ra < 400$, while S_2 and S_3 exist for $Ra \geq 76$ and $Ra \geq 172$, respectively. Hence, for $Ra < 76$, only a single steady state solution exists. This suggests that an improved and reproducible benchmark test case would be one whose Rayleigh number is such that $Ra < 76$. We constructed a test case for $Ra = 60$ in this lower Rayleigh number regime. For this new Low Rayleigh Number Elder Problem, results of the pseudospectral method were in excellent agreement with those produced using a conventional variable density groundwater flow and solute transport simulator. We provide new solutions for the alternative test case $Ra = 60$ and propose this as a new benchmark test case which avoids the multiple steady state solutions that exist for cases where $Ra > 76$. In this regime, both convective flow (albeit of reduced magnitude compared to $Ra = 400$ case) and diffusion/dispersion control solute transport processes are substantial, and thus the relevant physical processes are tested.

[48] It is noted that the original Elder problem with $Ra = 400$ can still be useful if taking into account the existence of several steady state solutions. A complete benchmark test for the Elder problem could consist of a series of Ra tests: (1) test $Ra = 0$ and compare to the given analytical solution, (2) test $Ra = 60$ and verify the unique steady state solution and the transients leading to it, and (3) run the original Elder problem at $Ra = 400$ and reproduce at least S_1 and S_2. A simulation code which is able to satisfy all three tests could be considered as sufficiently verified for the Elder problem.

[49] The use of pseudospectral methods appears promising in the solution of unstable free convective (gravitational instability) type problems. The absence of spatial discretization errors makes pseudospectral methods a preferred choice for studying convective instabilities. However, these methods will not be applicable to all instability problems, in particular those with complex geometries and mixed type boundary conditions. In these cases, finite volume, finite element or spectral element techniques are more suitable. Future studies should examine the wider applicability of pseudospectral methods in a range of other free convection type problems.

Appendix A: Chebyshev Polynomials and the Cosine Transform

[50] There is a wealth of information about spectral methods available in the literature and in textbooks. In particular the application of collocation methods (which are formulated in physical space and do not rely on FFTs) are well documented [*Trefethen*, 2000; *Weideman and Reddy*, 2001; *Fornberg*, 1996]. However, the collocation methods are limited to relatively few modes as the differentiation matrices are full; the computational requirements scale as $O(N^2)$. In contrast, FFT-based Chebyshev methods scale as $O(N \log N)$, which makes them the preferred choice for large problems. However, an exact method to implement Chebyshev methods using Fast Fourier Transforms (FFT) was not readily outlined in a single source. This appendix is intended as a very short introduction to using Chebyshev polynomials for differential equations with the FFT.

[51] At first sight the Chebyshev polynomials T_k in equation (19) seem to have little to do with trigonometric functions. However, the formal definition of T_k is [*Boyd*, 2001, p. 497]

$$T_k = \cos(k\theta) \tag{A1}$$

where $\theta = \arccos \xi$. We can immediately see that (A1) is identical to the first two terms of (19), as $T_0 = \cos 0 = 1$ and $T_1 = \cos(\arccos \xi) = \xi$. The recursion rule $T_{k+1} = 2\xi T_k - T_{k-1}$ can be obtained from substituting (A1) into the trigonometric identity

$$2\cos\theta\cos k\theta = \cos(k+1)\theta + \cos(k-1)\theta. \tag{A2}$$

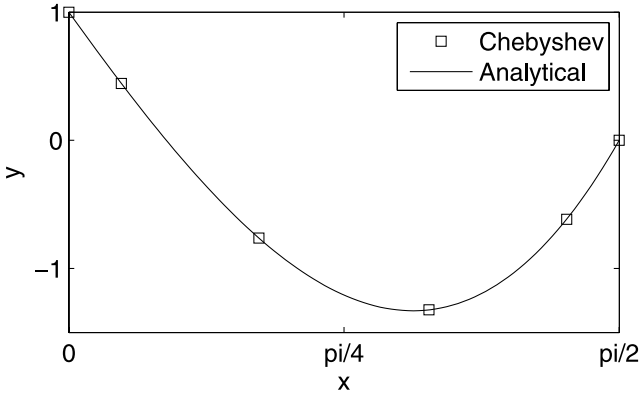

Figure A1. Solution of equation (8) with $N = 5$ Chebyshev polynomials.

which immediately results in $T_{k+1} = 2\,\xi\,T_k - T_{k\text{-}1}$. Note that (A1) indicates that the Chebyshev polynomials are nothing more than a cosine transform followed by a coordinate transform according to $\theta(\xi) = \arccos\,\xi$. Chebyshev polynomials are orthogonal with respect to the weighting function $1/\sqrt{1-\xi^2}$ (which originates from the coordinate transform):

$$\int_{-1}^{1} \frac{T_m T_n}{\sqrt{1-\xi^2}}\,d\xi = \frac{\pi}{2} c_n \delta_{mn}, \tag{A3}$$

where δ_{mn} is the Kronecker delta, $c_0 = 2$, and $c_n = 1$ for all $n > 0$. If the spacing of ξ is chosen according to the Chebyshev-Gauss-Lobatto points

$$\xi_n = \cos\left(\frac{n\pi}{N}\right), n = 0, 1, \ldots, N, \tag{A4}$$

then $\theta_n = \arccos\,\xi_n = n\pi/N$ is equidistant. Therefore, the Chebyshev expansion in equation (18) takes the form of a discrete cosine transform [*Boyd*, 2001, p. 46] and can be written as

$$p(\xi_n) = \sum_{k=0}^{N} \tilde{p}_k \cos k\theta_n. \tag{A5}$$

This property makes Chebyshev methods particularly attractive from a computational perspective, as the transformation from physical space to functional space can be efficiently carried out in $O(N \log N)$ operations using FFTs.

[52] The Chebyshev coefficients $\tilde{p}_k$ in equation (18) are related to the coefficients of the first derivative $\tilde{p}_k^{(1)}$ of equation (21) by a recurrence relation (in descending order) [*Boyd*, 2001, p. 177]

$$\begin{aligned} \tilde{p}_{N-1}^{(1)} &= \tilde{p}_N^{(1)} = 0 \\ \tilde{p}_{k-1}^{(1)} &= 2k\tilde{p}_k + \tilde{p}_{k+1}^{(1)} \\ 2\tilde{p}_0^{(1)} &= 2\tilde{p}_1 + \tilde{p}_2^{(1)} \end{aligned} \tag{A6}$$

This recurrence relation can be derived using (A1) and a trigonometric identity [e.g., *Johnson*, 1996, p. 13]. From (A6) it follows that the differentiation matrix $\mathbf{D}_\xi$, defined in equation (22), is given by

$$\mathbf{D}_\xi = \begin{bmatrix} 2 & 0 & -1 & & \\ 0 & 1 & \ddots & \ddots & \\ & \ddots & \ddots & \ddots & -1 \\ & & \ddots & \ddots & 0 \\ & & & 0 & 1 \end{bmatrix}^{-1} \begin{bmatrix} 0 & 2 & 0 & & \\ & \ddots & 4 & \ddots & \\ & & \ddots & \ddots & 0 \\ & & & \ddots & 2N \\ & & & & 0 \end{bmatrix} \tag{A7}$$

which results in (23) upon evaluation.

[53] The use of Chebyshev methods in differential equations will be demonstrated using a Helmholtz equation, which resembles the equation for the stream function (16):

$$\frac{d^2y}{dx^2} + y = 2e^x \tag{A8}$$

subject to $y(0) = 1$ and $y(\pi/2) = 0$. This differential equation has the exact solution $y = e^x - e^{\pi/2} \sin x$. As the Chebyshev polynomials are defined on $-1 \le \xi \le 1$, a change of variables as $x = \pi(\xi + 1)/4$ is used, which results in

$$\frac{16}{\pi^2}\frac{d^2y}{d\xi^2} + y = 2e^{\pi(\xi+1)/4} \tag{A9}$$

The Chebyshev polynomial coefficients for y, $d^2y/d\xi^2$ and $r = 2e^{\pi\ (\xi+1)/4}$ will be denoted by $\tilde{y}_k$, $\tilde{y}^{(2)}$ and $\tilde{r}_k$, respectively. Substituting the Chebyshev expansions into (A8), and invoking orthogonality of the basis functions, we obtain

$$\frac{16}{\pi^2}\tilde{y}_k^{(2)} + \tilde{y}_k = \tilde{r}_k. \tag{A10}$$

[54] As the vector $\tilde{\mathbf{y}}^{(2)} = [\tilde{y}_0^{(2)}, \ldots, \tilde{y}_N^{(2)}]^T$ is related to the vector $\tilde{\mathbf{y}} = [\tilde{y}_0, \ldots, \tilde{y}_N]^T$ by $\tilde{\mathbf{y}}^{(2)} = \mathbf{D}_\xi^2\,\tilde{\mathbf{y}}$, the resulting system of equations is

$$\mathbf{L}\tilde{\mathbf{y}} = \tilde{\mathbf{r}}, \tag{A11}$$

where $\mathbf{L} = \frac{16}{\pi^2}\,\mathbf{D}_\xi^2 + \mathbf{I}$ (note the correspondence to equation (25)).

[55] The boundary conditions are enforced via the tau method, i.e., by incorporating them in the last two rows of $\mathbf{L}$. This is permitted because the last two rows of $\mathbf{D}_\xi^2$ ordinarily contain zeros only. Observing that $T_k(\xi = -1) = (-1)^k$ and $T_k(\xi = 1) = 1$, we set $L_{N,k} = (-1)^k$, $L_{N+1,k} = 1$, $R_N = 1$, and $R_{N+1} = 0$. The Chebyshev solution can now be determined via $\tilde{\mathbf{y}} = \mathbf{L}^{-1}\,\tilde{\mathbf{r}}$.

[56] For further clarification concerning the relation between the Chebyshev polynomials and the FFT, consider the small code fragment which implements the solution of (A8) using Chebyshev polynomials in MATLAB, given below. This fragment includes the construction of the differentiation matrix, the forward and inverse cosine transforms, applying the prefactors, the solution of the system, and the comparison with the analytical solution. The result for $N = 5$ polynomials is shown in Figure A1. Clearly, even with so few modes, the Chebyshev solution is practically indistinguishable from the analytical solution.

```
N = 5;%Set number of polynomials
xi = [cos(linspace(0, pi, N + 1))]';
     %Lobatto points
A = spdiags([[2;ones(N, 1)], -ones(N + 1, 1)],
     [0 2], N + 1, N + 1);
B = spdiags([0;2*[1:N]';0], 1, N + 1, N + 1);
Dxi = inv(A)*B;%Create differentiation matrix
x = (xi + 1)*pi/4; Dx = Dxi*4/pi;
     %Transform to 0 < x < pi/2
L = Dx^2 + speye(N + 1, N + 1);%Form LHS
L(N, :) = (-1).^[0:N];L(N + 1, :)
     = ones(1, N + 1);%Set BCs
r = 2*exp(x);%RHS of Helmholtz eqn.
rt = real(fft([r;r(N:-1:2)]));
     rt = rt(1:N + 1);%DCT-I
rt = rt/N; rt([1 N + 1]) = rt([1 N + 1])/2;
     %Prefactors
rt([N;N + 1]) = [1;0];%Set RHS of BCs
yt = inv(L)*rt;%Solve Helmholtz eqn
yt([1 N + 1]) = yt([1 N + 1])*2;%Prefactors
y = real(fft([yt;yt(N:-1:2)]));
     y = y(1:N + 1)/2; %IDCT-I
xx = linspace(0, pi/2, 100);
f = exp(xx) - exp(pi/2)*sin(xx);%Analytical sol.
plot(x, y, 'ks',xx, f, 'k-');
     legend('Cheb.', 'An.');
```

Appendix B: Influence of *d*

[57] It may be questioned what the effect is of varying d in equation (26) on the transients and the steady state solutions of the Elder problem. We find that the transients are very sensitive to d [see also *Woods and Carey*, 2007]. As the transients ultimately determine the final steady state, d influences whether the system will end up in S_1, S_2 or S_3. However, once a steady state solution is obtained, varying d only changes the solution near the transition. Indeed, all three steady state solutions at $Ra = 400$ are stable for $d = 0.05$, $d = 0.10$, and $d = 0.20$, which represent sharp to rather smooth transitions (see also Figure 2). The bifurcation points have a small dependence on d; for larger d, S_2 and S_3 come into existence at slightly higher Ra.

[58] Below we study the effect of d on the local Sherwood number Sh_x. In Table B1, resolutions are given for simulations with $d = 0.05$, $d = 0.10$ and $d = 0.20$. The resolution for each simulation is chosen such that the solutions are pointwise converged. From Table B1 it is clear that as d becomes smaller, the required resolution for pointwise convergence quickly increases: halving d requires doubling of the resolution.

Table B1. Resolution Requirements for Pointwise Convergence at Various d

d	N_x	N_y
0.05	513	129
0.10	257	65
0.20	129	65

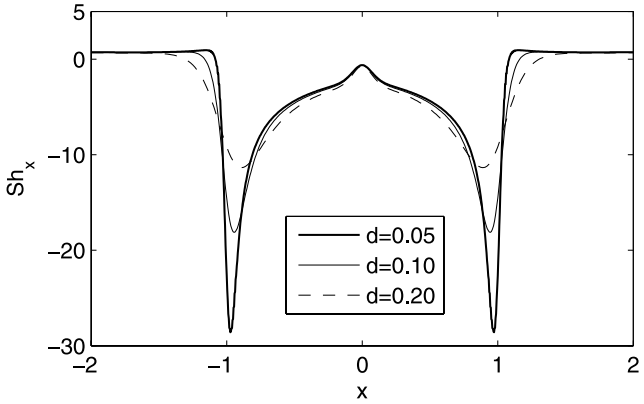

Figure B1. The vertical solute flux Sh_x for various d.

[59] Shown in Figure B1 is Sh_x as defined in (28) as a function of d. Clearly, as d becomes smaller, the local vertical solute flux Sh_x rapidly becomes very peaked, and consequently difficult to solve. In the limit of $d \to 0$, this peak will become a singularity.

[60] Although d dramatically affects the peak in Sh_x at $x = 1$ and $x = 3$, it is important to note that the effect of d is predominantly local; for $-0.8 < x < 0.8$, Sh_x is virtually unaffected by the variations in d. As a consequence, if d is sufficiently small, the solution away from the transition is converged while the details near $x = \pm 1$ may still change upon varying d. At $d = 0.05$, the solution away from the transition is sufficiently converged, as can be judged by the marginal differences between $d = 0.10$ and $d = 0.05$.

Appendix C: Solution for Zero *Ra*

[61] Setting $Ra = 0$ and applying the Fourier cosine transform

$$\hat{c}_0 = \frac{1}{2}\int_0^2 c(x)dx \tag{C1}$$

$$\hat{c}_m = \int_0^2 c(x)\cos(g_m x)dx, \quad g_m = m\pi/2 \tag{C2}$$

which has the inverse

$$c(x) = \hat{c}_0 + \sum_{m=1}^{\infty} \hat{c}_m \cos(g_m x) \tag{C3}$$

and the Laplace transform

$$\overline{c}(s) = \int_0^{\infty} c(t)\exp(-st)dt \tag{C4}$$

to equations (2) to (7) leads to the ordinary differential equation

$$\frac{d^2\overline{\hat{c}}_m}{dz^2} = \lambda_m^2 \overline{\hat{c}}_m, \quad \lambda_m^2 = g_m^2 + s \tag{C5}$$

which has the general solution

$$\overline{\hat{c}}_m(z,s) = A_m \cosh(\lambda_m y) + B_m \sinh(\lambda_m z) \tag{C6}$$

[62] From the lower boundary condition $A_m = 0$. The B_m coefficients are obtained by applying equations (C2) and (C3) at $z = 1$ (recall equation (8)) such that

$$B_0 \sinh\left(s^{1/2}\right) = \frac{1}{2s} \int_0^1 dy = \frac{1}{2s} \tag{C7}$$

$$B_m \sinh(\lambda_m) = \frac{1}{s} \int_0^1 \cos(g_m y) dy = \frac{1}{s g_m} \sin(g_m) \tag{C8}$$

therefore

$$\overline{c}(x,z,s) = \frac{\sinh\left(s^{1/2} z\right)}{2s \sinh\left(s^{1/2}\right)} + \sum_{m=1}^{\infty} \frac{\sin(g_m) \sinh(\lambda_m z) \cos(g_m x)}{s g_m \sinh(\lambda_m)} \tag{C9}$$

which can be inverted numerically using the *Stehfest* [1970] algorithm [see also *Valko and Abate*, 2004].

[63] Also note that application of the Tauberian theorem [e.g., *Wylie and Barrett*, 1982, p. 420] leads to the steady state solution

$$\lim_{s \to 0} s\overline{c}(x,z,s) = \frac{z}{2} + \sum_{m=1}^{\infty} \frac{\sin(g_m) \sinh(g_m z) \cos(g_m x)}{g_m \sinh(g_m)} \tag{C10}$$

[64] **Acknowledgments.** This project was partially funded by the WorleyParsons EcoNomicsTM initiative.

References

Ackerer, P., A. Younes, and R. Mose (1999), Modeling variable density flow and solute transport in porous medium: 1. Numerical model and verification, *Transp. Porous Media*, *35*, 345–373, doi:10.1023/A:1006564309167.

Al-Maktoumi, A., D. A. Lockington, and R. E. Volker (2007), SEAWAT 2000: Modelling unstable flow and sensitivity to discretization levels and numerical schemes, *Hydrogeol. J.*, *15*, 1119–1129, doi:10.1007/s10040-007-0164-2.

Bear, J., and G. Dagan (1964), Some exact solutions of interface problems by means of the hodograph method, *J. Geophys. Res.*, *69*, 1563–1572.

Bolster, D. T., D. M. Tartakovsky, and M. Dentz (2007), Analytical models of contaminant transport in coastal aquifers, *Adv. Water Resour.*, *30*, 1962–1972, doi:10.1016/j.advwatres.2007.03.007.

Boufadel, M., M. Suidan, and A. Venosa (1999), Numerical modeling of water flow below dry salt lakes: Effect of capillarity and viscosity, *J. Hydrol.*, *221*, 55–74, doi:10.1016/S0022-1694(99)00077-3.

Boyd, J. P. (2001), *Chebyshev and Fourier Spectral Methods*, Dover, New York.

Dentz, M., D. M. Tartakovsky, E. Abarca, A. Guadagnini, X. Sanchez-Vila, and J. Carrera (2006), Variable density flow in porous media, *J. Fluid Mech.*, *561*, 209–235, doi:10.1017/S0022112006000668.

Diersch, H. J. G. (2005), *FEFLOW Reference Manual*, Inst. for Water Resour. Plann. and Syst. Res., Berlin.

Diersch, H. J., and O. Kolditz (2002), Variable-density flow and transport in porous media: Approaches and challenges, *Adv. Water Resour.*, *25*, 899–944, doi:10.1016/S0309-1708(02)00063-5.

Elder, J. (1967), Transient convection in a porous medium, *J. Fluid Mech.*, *27*, 609–623, doi:10.1017/S0022112067000576.

Farajzadeh, R., H. Salimi, P. L. J. Zitha, and H. Bruining (2007), Numerical simulation of density-driven natural convection in porous media with application for CO_2 injection projects, *Int. J. Heat Mass Transfer*, *50*, 5054–5064, doi:10.1016/j.ijheatmasstransfer.2007.08.019.

Fornberg, B. (1996), *A Practical Guide to Spectral Methods*, Cambridge Univ. Press, Cambridge, U. K.

Frisch, U. (1995), *Turbulence*, Cambridge Univ. Press, Cambridge, U. K.

Frolkovic, P., and H. de Schepper (2000), Numerical modelling of convection dominated transport coupled with density driven flow in porous media, *Adv. Water Resour.*, *24*, 63–72, doi:10.1016/S0309-1708(00)00025-7.

Goswami, R. R., and T. P. Clement (2007), Laboratory-scale investigation of saltwater intrusion dynamics, *Water Resour. Res.*, *43*, W04418, doi:10.1029/2006WR005151.

Hassanzadeh, H., M. Pooladi-Darvish, and D. W. Keith (2007), Scaling behavior of convective mixing, with application to geological storage of CO_2, *AIChE J.*, *53*, 1121–1131, doi:10.1002/aic.11157.

Henry, H. R. (1964), Effects of dispersion on salt encroachment in coastal aquifers, *U.S. Geol. Surv. Water Supply Pap.*, *1613-C*.

Holzbecher, E. (1998), *Modelling Density-Driven Flow in Porous Media*, Springer, Berlin.

Horton, C. W., and F. T. Rogers (1945), Convection currents in a porous medium, *J. Appl. Phys.*, *16*, 367–370, doi:10.1063/1.1707601.

Huppert, H. E., and A. W. Woods (1995), Gravity-driven flows in porous layers, *J. Fluid Mech.*, *292*, 55–69, doi:10.1017/S0022112095001431.

Hussaini, M. Y., and T. A. Zang (1987), Spectral methods in fluid-dynamics, *Annu. Rev. Fluid Mech.*, *19*, 339–367.

Johannsen, K. (2003), On the validity of the Boussinesq approximation for the Elder problem, *Comput. Geosci.*, *7*, 169–182, doi:10.1023/A:1025515229807.

Johnson, D. (1996), Chebyshev polynomials in the spectral tau method and applications to eigenvalue problems, *NASA Tech., 198451*.

Kacimov, A. R., and Y. V. Obnosov (2001), Analytical solution for a sharp interface problem in sea water intrusion into a coastal aquifer, *Proc. R. Soc. London, Ser. A*, *457*, 3023–3038, doi:10.1098/rspa.2001.0857.

Kolditz, O., R. Ratke, H. J. Diersch, and W. Zielke (1997), Coupled groundwater flow and transport: 1. Verification of variable density flow and transport models, *Adv. Water Resour.*, *21*, 27–46, doi:10.1016/S0309-1708(96)00034-6.

Lin, J., J. B. Snodsmith, and C. Zheng (2009), A modeling study of seawater intrusion in Alabama Gulf Coast, USA, *Environ. Geol.*, *57*, 119–130, doi:10.1007/s00254-008-1288-y.

Martucci, S. A. (1994), Symmetric convolution and the discrete sine and cosine transform, *IEEE Trans. Signal Process.*, *42*, 1038–1051, doi:10.1109/78.295213.

Narayan, K. A., C. Schleeberger, and K. L. Bristow (2007), Modelling seawater intrusion in the Burdekin Delta Irrigation Area, North Queensland, Australia, *Agric. Water Manage.*, *89*, 217–228, doi:10.1016/j.agwat.2007.01.008.

Oldenburg, C. M., and K. Pruess (1995), Dispersive transport dynamics in a strongly coupled groundwater-brine flow system, *Water Resour. Res.*, *31*, 289–302.

Oltean, C., and M. A. Bues (2001), Coupled groundwater flow and transport in porous media: A conservative or non-conservative form?, *Transp. Porous Media*, *44*, 219–246, doi:10.1023/A:1010778224076.

Park, C. H., and M. M. Aral (2007), Sensitivity of the solution of the Elder problem to density, velocity and numerical perturbations, *J. Contam. Hydrol.*, *92*, 33–49, doi:10.1016/j.jconhyd.2006.11.008.

Park, N. (1996), Closed-form solutions for steady state density-dependent flow and transport in a vertical soil column, *Water Resour. Res.*, *32*, 1317–1322.

Riaz, A., M. Hesse, H. A. Tchelepi, and F. M. Orr Jr. (2006), Onset of convection in a gravitationally unstable, diffusive boundary layer in porous media, *J. Fluid Mech.*, *548*, 87–111, doi:10.1017/S0022112005007494.

Shampine, L. F., and M. W. Reichelt (1997), The MATLAB ODE Suite, *SIAM J. Sci. Comput.*, *18*, 1–22, doi:10.1137/S1064827594276424.

Shampine, L. F., M. W. Reichelt, and J. A. Kierzenka (1999), Solving index-1 DAEs in MATLAB and Simulink, *SIAM J. Sci. Comput.*, *41*, 538–552, doi:10.1137/S003614459933425X.

Simmons, C. T. (2005), Variable density groundwater flow: From current challenges to future possibilities, *Hydrogeol. J.*, *13*, 116–119, doi:10.1007/s10040-004-0408-3.

Simmons, C. T., K. A. Narayan, and R. A. Wooding (1999), On a test case for density-dependent groundwater flow and solute transport models: The salt lake problem, *Water Resour. Res.*, *35*, 3607–3620.

Simpson, M. J., and T. P. Clement (2003), Theoretical analysis of the worthiness of Henry and Elder problems as benchmarks of density dependent groundwater flow models, *Adv. Water Resour.*, *26*, 17–31, doi:10.1016/S0309-1708(02)00085-4.

Simpson, M. J., and T. P. Clement (2004), Improving the worthiness of the Henry problem as a benchmark for density-dependent groundwater flow models, *Water Resour. Res.*, *40*, W01504, doi:10.1029/2003WR002199.

Soto Meca, A., F. Alhama, and C. F. Gonzalez Fernandez (2007), An efficient model for solving density driven groundwater flow problems based on the network simulation method, *J. Hydrol.*, *339*, 39–53, doi:10.1016/j.jhydrol.2007.03.003.

Stehfest, H. (1970), Algorithm 368: Numerical inversion of Laplace transforms [D5], *Commun. ACM*, *13*, 47–49, doi:10.1145/361953.361969.

Trefethen, L. N. (2000), *Spectral Methods in Matlab*, Soc. for Ind. and Appl. Math., Philadelphia, Pa.

Valko, P. P., and J. Abate (2004), Comparison of sequence accelerators for the Gaver method of numerical Laplace transform inversion, *Comput. Math. Appl.*, *48*, 629–636, doi:10.1016/j.camwa.2002.10.017.

Voss, C. I., and W. R. Souza (1987), Variable density flow and solute transport simulation of regional aquifers containing a narrow freshwater-saltwater transition zone, *Water Resour. Res.*, *23*, 1851–1866.

Weideman, J. A. C., and S. C. Reddy (2001), A MATLAB differentiation matrix suite, *Trans. Math. Software*, *26*, 465–519, doi:10.1145/365723.365727.

Wooding, R. A. (2007), Variable-density saturated flow with modified Darcy's law: The salt lake problem and circulation, *Water Resour. Res.*, *43*, W02429, doi:10.1029/2005WR004377.

Wooding, R. A., S. W. Tyler, I. White, and P. A. Anderson (1997), Convection in groundwater below an evaporating salt lake: 2. Evolution of fingers or plumes, *Water Resour. Res.*, *33*, 1219–1228.

Woods, J. A., and G. F. Carey (2007), Upwelling and downwelling behavior in the Elder-Voss-Souza benchmark, *Water Resour. Res.*, *43*, W12403, doi:10.1029/2006WR004918.

Woods, J. A., M. D. Teubner, C. T. Simmons, and K. A. Narayan (2003), Numerical error in groundwater flow and solute transport simulation, *Water Resour. Res.*, *39*(6), 1158, doi:10.1029/2001WR000586.

Wylie, C. R., and L. C. Barrett (1982), *Advanced Engineering Mathematics*, McGraw-Hill, New York.

Zimmermann, S., P. Bauer, R. Held, W. Kinzelbach, and J. H. Walther (2006), Salt transport on islands in the Okavango Delta: Numerical investigations, *Adv. Water Resour.*, *29*, 11–29, doi:10.1016/j.advwatres.2005.04.013.

S. A. Mathias and M. van Reeuwijk, Department of Civil and Environmental Engineering, Imperial College London, London SW7 2AZ, UK. (m.vanreeuwijk@imperial.ac.uk)

C. T. Simmons and J. D. Ward, School of Chemistry, Physics and Earth Sciences, Flinders University, P.O. Box 2100, Adelaide, SA 5001, Australia.